CHAPTER 3

MAGNETIC NANOPARTICLES: SYNTHESIS, CHARACTERIZATION AND APPLICATIONS

MAGNETIC NANOPARTICLES: SYNTHESIS, CHARACTERIZATION AND APPLICATIONS

3.1 Introduction

Nanoparticle (NP) based imaging probes are rapidly emerging as a plausible alternative to the conventionally available molecular probes. Such nanomaterials provide the scope of synthesis and development of an extensive range of products for biomedical applications like imaging and diagnostic procedures and drug delivery [1-6]. The property of the nanosystem varies from the bulk due to their higher surface area per unit volume and contribution from surface chemistry such as ligand arrangement. Monodisperse hydrophilic MNPs with low retentivity or superparamagnetism are the required primary features of these MNPs for biomedical applications. The surge in efforts to develop non-invasive/non-surgical methods for the detection and diagnostic applications has led to rapid developments in the field of Magnetic Resonance Imaging (MRI). The major advantage of MRI is the use of non-ionizing energy for high spatial resolution, which can be further boosted by the use of magnetic nanomaterials, leading to the shortening of the proton relaxation time (T_1 and/or T_2) [7-10].

Iron oxide nanoparticles (NPs) with controlled microstructure and high magnetization have potential for numerous *in vivo* applications, such as Magnetic Resonance Imaging (MRI) contrast improvement, stem cell labeling for *in vivo* tracking, hyperthermia, and drug delivery [11-15]. Several methods have been reported for the Fe_3O_4 nanoparticles synthesis such as solvothermal method, a sol-gel method, and miniemulsion polymerization method [16-19].

FePt based nanosystem offers a wide range of magnetic properties and possess high magnetic moment [20]. FePt MNPs are generally reported to be synthesized through hydrophobic capping [21-23]. To make them amenable for biomedical applications, a second step is introduced to convert these MNPs into hydrophilic nature. The hydrophilicity is achieved, in these cases, either by ligand exchange or coating of the hydrophobic MNPs by a hydrophilic capping agent [24-29]. The major concern associated with this additional step is an aggregation of MNPs or coalescence during the process or alteration of intrinsic properties. Although the potency of FePt MNPs was realized years back, little attention has been paid for developing hydrophilic, superparamagnetic, iron-platinum (FePt) MNPs for biomedical application through direct synthesis route [30]. In this regard, a one pot direct synthesis technique of hydrophilic FePt MNPs capped with thioglycolic acid is synthesized [31]. Indeed, it is interesting to understand the synthesis process as well as the results, which is suitable for our purposes.

In our study, development of magnetite (Fe_3O_4) and Iron-Platinum (FePt) MNPs for MR imaging application has been discussed in details. In this regard, a new, simple, open environment synthesis, using a non-aqueous thermal decomposition method without any reducing agent, has been used for obtaining crystalline superparamagnetic magnetite NPs. Using a ligand exchange process by TMAOH, Fe_3O_4 was transformed to hydrophilic and used for MR imaging application. On the other side, the so prepared TMAOH capped crystalline FePt nanodots and as prepared TGA capped FePt MNPs are synthesized by the polyol process. A comprehensive study on the development of these MNPs and formation mechanism has been carried out for better understanding of the structure-property correlation. The Fe_3O_4 and FePt MNPs exhibit superior contrast property for MR imaging.

3.2 Materials and methods

This section explains about the materials and the processes applied for the synthesis of IO@S (Fe_3O_4@steraric Acid), IO@T (Fe_3O_4@tetramethylammonium hydroxide), FePt@OO (FePt@oleic acid & oleyamine) & FePt@T (FePt @tetramethylammonium hydroxide) and FePt@TGA (FePt@thioglycolic acid) nanoparticles.

Synthesis of magnetite nanoparticles

The precursors, iron (III) acetylacetonate (Fe $(acac)_3$) and stearic acid, were procured from Sigma-Aldrich and Lobachemie reagent respectively. Tetramethylammonium hydroxide (TMAOH, 25%) was obtained from Merck Chemicals (Mumbai, India). The water used in the experiments was from a Milli-Q system (Milli-Q Academic, Millipore, France). The thermal decomposition and ligand exchange process were used for the synthesis of hydrophilic magnetite nanoparticles.

Two pot synthesis of hydrophilic FePt nanoparticles

For the synthesis, the precursors, platinum (II) acetylacetonate (Pt $(acac)_2$), oleic acid ($C_{18}H_{34}O_2$) and oleylamine ($C_{18}H_{37}N$) were procured from Sigma-Aldrich. Iron (III) nitrate nonahydrate ($Fe(NO_3)_3.9H_2O$), sodium borohydride ($NaBH_4$), ethylene glycol ($C_2H_6O_2$) and tetramethylammonium hydroxide (TMAOH, 25%) were obtained from Merck Chemicals (Mumbai, India). Type 1 water (resistivity > 18 Mɋ -cm at 25 °C, bacteria count < 10 CFU/ml, endotoxin < 0.03 EU/ml) of Milli-Q purification system was used for purification, characterization, and experimental processes. The hydrophilic FePt nanoparticles were synthesized using polyol process and ligand exchange mechanism.

One pot synthesis of FePt nanoparticles (FePt@TGA)

The analytical grade materials were used in the synthesis and purification procedure of FePt@TGA nanoparticles. The metallic precursor Pt (II) acetylacetonate [$Pt(acac)_2$, 99.99%] and Fe (III) acetylacetonate [$Fe(acac)_3$, 99.95%] were procured from Sigma-Aldrich. The reducing and capping agents used in the reactions were sodium borohydride ($NaBH_4$) and thioglycolic acid (TGA, 80%) respectively, procured from Merck Millipore. The ethylene glycol ($C_2H_6O_2$) used as a solvent and ethyl alcohol, acetone used for the purification process, were procured from Merck Millipore. Type 1 water of Milli-Q purification system was used for purification, characterization, and experimental processes. The polyol process used for the synthesis of hydrophilic FePt nanoparticles.

Section-A

3.3 Synthesis and surface modification of stearic acid capped of magnetite nanoparticles

Fe_3O_4 NPs have been synthesized by thermal decomposition of iron (III) acetylacetonate [$Fe(C_5H_7O_2)_3$] in solution in stearic acid which acts as a solvent as well as the capping agent. Initially, iron (III) acetylacetonate was added into molten stearic acid at 70°C with continuous stirring and heated up to 180 °C at the rate of 1°C/minute until the viscous mass turned black. The cooled product was mechanically crushed into powder and purified by washing with tetrahydrofuran, chloroform, and ethanol (ratio 3:1:1) solution three times. The so obtained NPs (IO@S) collected after centrifugation was dried in an air oven. The transformation of IO@S to hydrophilic NPs was carried out by dissolving 150 mg of NPs in 6 mL of 10 wt. % aqueous tetramethylammonium hydroxide (TMAOH) solution, followed by sonication. The resultant mixture was purified by washing with acetone, ethanol and Milli-Q water (ratio 8:1:1) solution two times. The so obtained (IO@T) magnetite NPs were finally dispersed in Milli-Q water for further characterization. **Figure 3.1** represents the schematic diagram of synthesis and ligand exchange of magnetite nanoparticles.

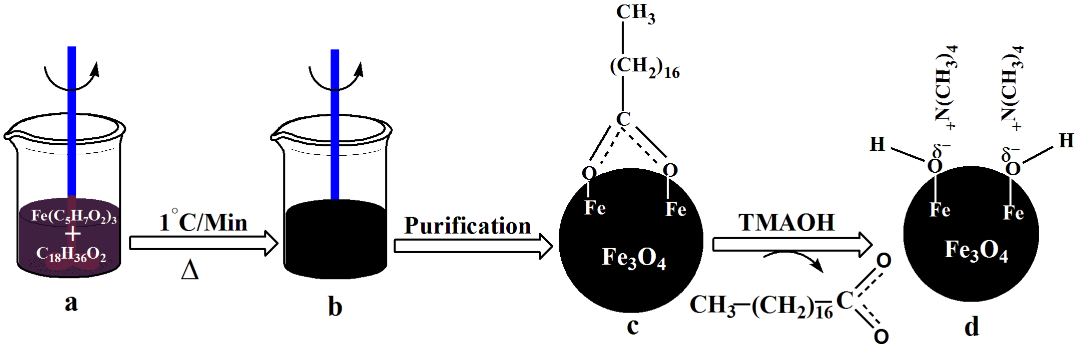

Figure 3.1 Schematic diagram represents the synthesis (a-c) and ligand exchange (d) of magnetite nanoparticles

3.4 Characterizations

The synthesized nanosystem was characterized using several characterization methods for understanding the properties of the nanosystems.

3.4.1 Results and discussion

The representative TEM micrographs of IO@S and IO@T (**figure 3.2 (a)** and **(b)**) are showing almost same microstructural characteristics of NPs. The particle size distribution (Figure **3.2 c**) of IO@T NPs reveals a very narrow size distribution, in the range 5 to 9 nm, with average particle size 7 nm. The XRD patterns of IO@S and IO@T shown in **figure 3.1 (d)** exhibiting the same diffraction peaks, (220), (311), (511) and (440) planes of magnetite (PDF No.-89-0688) indicates that the crystallographic phase of NPs has not been changed by TMAOH treatment.

The HRTEM micrograph (**figure 3.2 (e)**) of IO@T sample shows a crystal plane distance of 0.253 nm in (311) plane of magnetite. **Figure 3.2 (f)** shows magnetic hysteresis curves of IO@S and IO@T NPs, which exhibits smaller saturation magnetization 21.2 and 40.0 emu g^{-1}, respectively, than bulk magnetite [32]. Left upper inset shows magnetic moment vs. temperature (ZFC and FC) of IO@T sample up to 300 K and exhibits a blocking temperature ╔140K confirming superparamagnetic characteristics of the NPs.

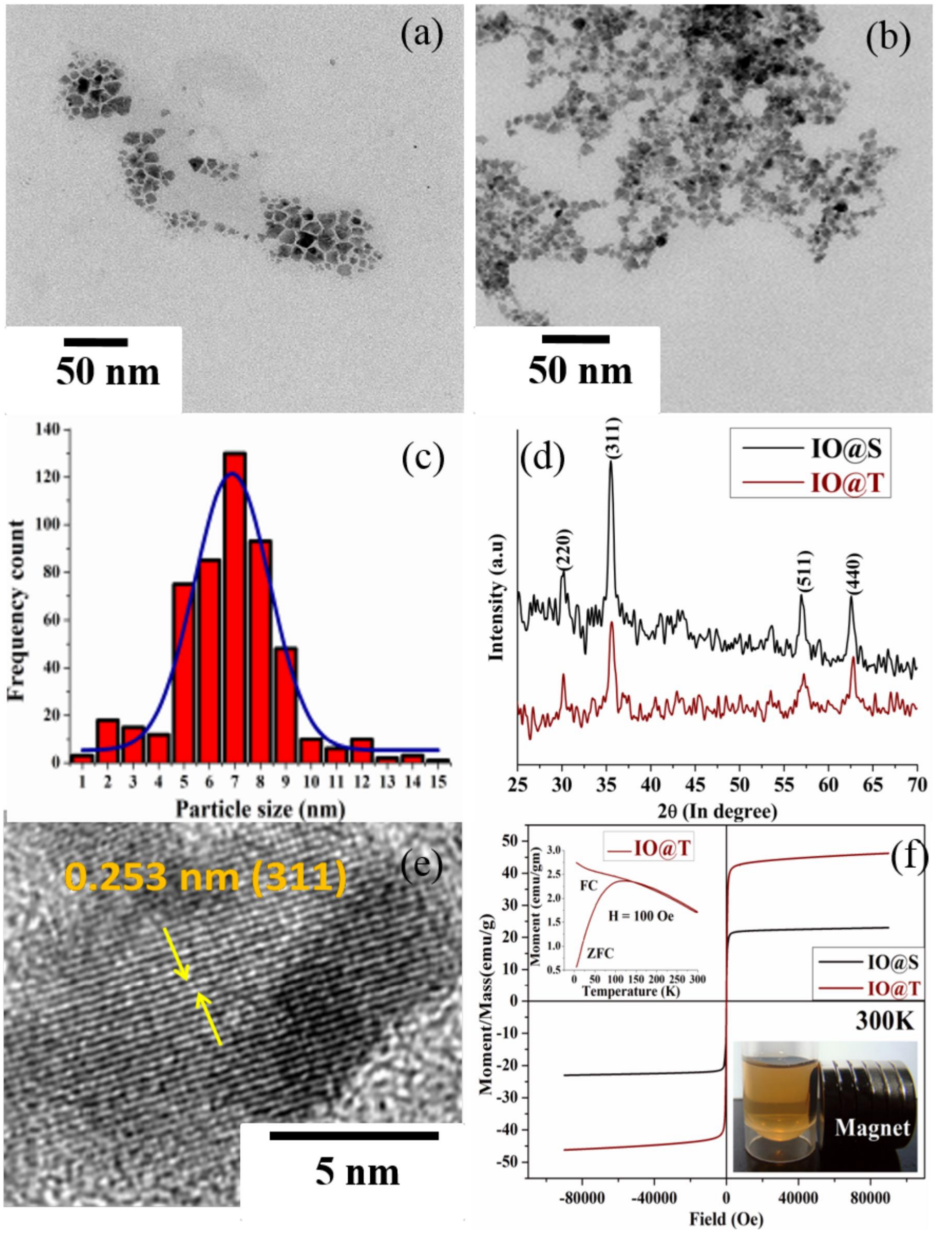

Figure 3.2 TEM micrographs of IO@S and IO@T are shown in (a) and (b), respectively, while (c) shows the particle size distribution profile of IO@T NPs, (d)

XRD pattern of IO@S and IO@T, (e) high resolution TEM image of IO@T NPs, (f) magnetic hysteresis loop of IO@S and IO@T NPs at room temperature. Left upper inset shows magnetic moment vs temperature for zero-field-cooling (ZFC) and field-cooling (FC) of IO@T sample. The right lower inset shows IO@T NPs behavior under magnetic field

Comparative FTIR spectra are shown in (**figure 3.3**) whereas inset reveals the differences of phase shift of IO@S NPs. In IO@S C-H asymmetrical and symmetrical stretching vibration are observed at around 2922 and 2853 cm^{-1} respectively. The carboxylate anion (COO^-) asymmetric and symmetric stretching vibrations are observed at around 1551 and 1433 cm^{-1} respectively [33]. In IO@T FTIR spectrum, the bands around 2922, 1472 cm^{-1} are assigned to the C-H and CH_3 antisymmetric stretching and bending vibrations respectively. The peak at 945 cm^{-1} might indicate the adsorption of $N(CH_3)_4OH$ on Fe_3O_4 [34, 35]. The signature peak, due to Fe-O bond vibration in IR spectrum of magnetite NPs and ɔ-Fe_2O_3 NPs, appears around 580 cm^{-1} and 630 and/or 573 cm^{-1} respectively [36]. The experimental result shows the peak of Fe-O bond vibration at around 580 cm^{-1} in both the spectra. It gives clear evidence that particles are predominantly in magnetite phase even after TMAOH treatment. The X-ray photoelectron spectroscopy (XPS) of stearic and TMAOH coated magnetite NPs are discussed in **3.1A** of **appendix–A**. XPS result confirms the surface modification and magnetite phase of the NPs.

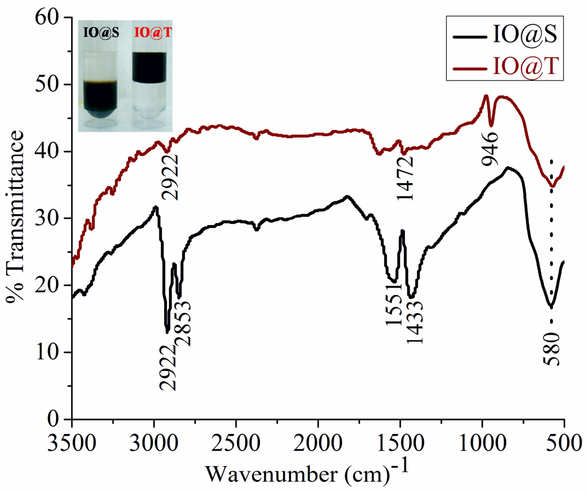

Figure 3.3 FTIR spectra of IO@S and IO@T Fe_3O_4 NPs. Inset: Photos of particle distribution between chloroform (bottom) and water (top)

The MR images of microfuge tube containing magnetite at concentration 0.9 µg/ml at selected echo times are depicted in **figure 3.4 (a)**. The plots of MRI signal intensities with echo time at a different concentration of magnetite are presented in **figure 3.4 (b).** The transverse relaxation time (T_2) of water was obtained by analyzing the signal intensity versus echo time curve by a mono-exponential function [$S_{TE}=S_{TE=0}$ (e^{-TE/T_2})]. The transverse relaxation rate, R_2 was obtained as $R_2 = 1/T_2$. The transverse relaxivity (r_2) obtained by linear analysis of relaxation rate versus magnetite NPs concentration plot was found to be 3.82 mL μg^{-1} s^{-1}. R_2 increases linearly with an increase in concentration as observed in **figure 3.4 (c)**. This relaxivity shows a significant improvement over commercially available iron oxide particles, where values ~ 1.6 mL $\mu g^{-1} s^{-1}$ has been reported [37].

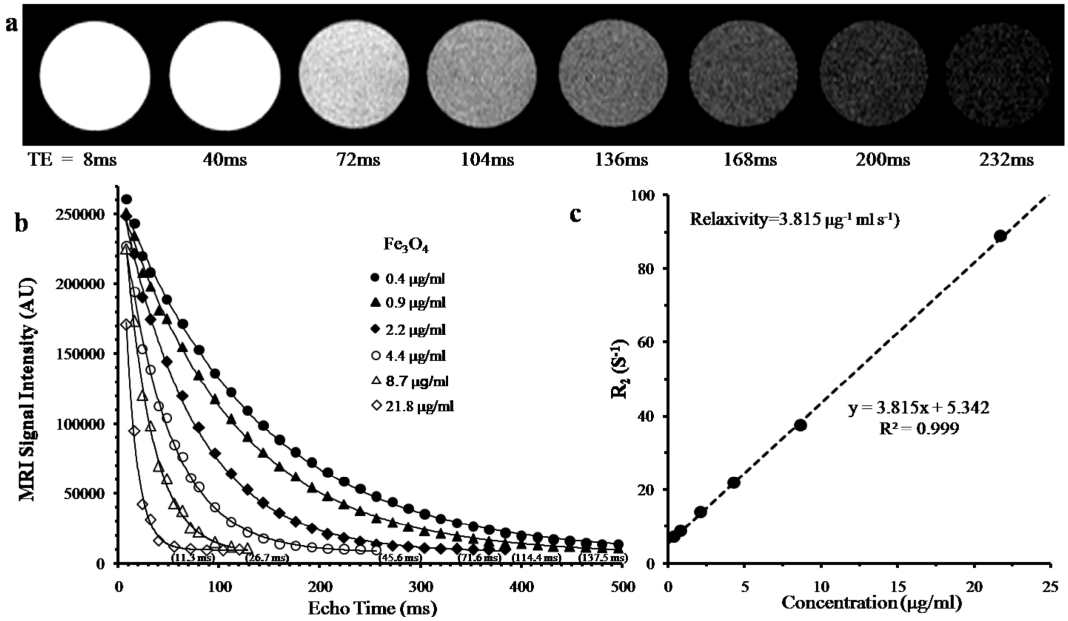

Figure 3.4 Transverse relaxivity of magnetite NPs. (a) The axial image of microfuge tube filled with magnetite solution (0.9 µg/ml.), (b) the variation of MR signal intensity with echo time at a different concentration of magnetite NPs. Numbers in parenthesis below each curve represent the T_2 value and (c) variation of transverse relaxation rate (R_2) with a concentration of magnetite NPs. The slope indicates the relaxivity of the magnetite.

Section-B

3.5 Synthesis and surface modification of oleic acid and oleylamine capped of FePt nanoparticles

A facile polyol process was suitably modified for the synthesis of hydrophobic FePt nanodots [38]. For synthesis, the precursors, 0.5 mmol platinum (II) acetylacetonate (Pt (acac)$_2$), 2 mmol iron (III) nitrate nonahydrate ($Fe(NO_3)_3.9H_2O$), 1 mmol sodium borohydride ($NaBH_4$), 0.5 mmol oleic acid ($C_{18}H_{34}O_2$) and 0.5 mmol oleylamine ($C_{18}H_{37}N$) were added with 15 ml of ethylene glycol ($C_2H_6O_2$), in three-necked flask, under nitrogen atmosphere at room temperature and heated in an oil-bath up to 180°C with a controlled heating rate of 5°C min^{-1}, leading to progressive change in coloration from yellow to a blackish precipitated form. The FePt precipitate was separated from the reaction mixture by centrifugation several times using ethyl alcohol and hexane to remove the residual surfactants. The purified FePt nanodots were finally re-suspended in hexane owing to its hydrophobic surface character.

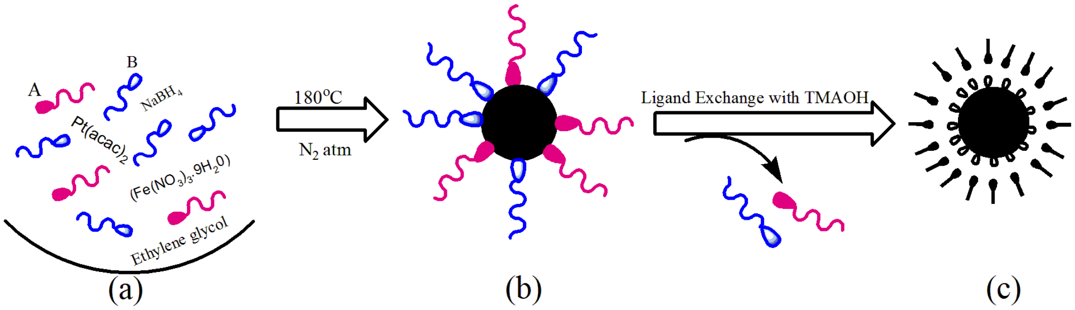

Figure 3.5 Schematic diagram represents the synthesis and ligand exchange of FePt nanodots. (a) Precursors [Oleic acid (A) and Oleylamine (B)], (b) Oleic acid and Oleylamine@ FePt and (c) TMAOH @ FePt . The surface capping is composed of (OH^-) anions (○) and ($(CH_3)_4N^+$) cations (—●)

The phase transformation from hydrophobic to hydrophilic was carried out with the help of ligand exchange process mediated by tetramethylammonium hydroxide ($(CH_3)_4NOH$). The transformation of hydrophobic FePt to hydrophilic FePt NPs was carried out by dissolving 150 mg powder of hydrophobic FePt NPs in 6 mL of 10 wt. % aqueous tetramethylammonium hydroxide (TMAOH) solution, followed by 20-minutes sonication at room temperature. The resultant mixture was purified by washing with acetone, ethanol and Milli-Q water (ratio 10:1:1) solution two times [39]. The TMAOH coating of FePt nanodots enables formation of a bilayer of hydroxide anions (OH^-) and tetramethylammonium cation ($(CH_3)_4N^+$) which creates electrostatic interparticle repulsion in an aqueous medium [40]. The so prepared nanodots were finally dissolved in 0.01 wt % TMAOH aqueous solution to obtain the ferrofluid. The schematic representation of the synthesis and ligand exchange of FePt nanodots is represented in **figure 3.5**.

3.6 Characterizations

The synthesized nanosystem was characterized using several characterization methods for understanding the properties of the nanosystems.

3.6.1 Results and discussion

Figure 3.6 shows the comparative FTIR spectra of hydrophobic (oleic acid and oleylamine capped) FePt nanodots and hydrophilic (TMAOH modified) FePt nanodots. The FTIR peaks at 2850 and 2924 cm^{-1} are due to the symmetric and asymmetric CH_2 stretching mode of an oleyl group respectively. The peak at 1638 cm^{-1} are due to the ɔ(C=C) stretch mode. The presence of $-COO^-$ asymmetric and symmetric stretching vibrations are observed at 1530 and 1440 cm^{-1}.

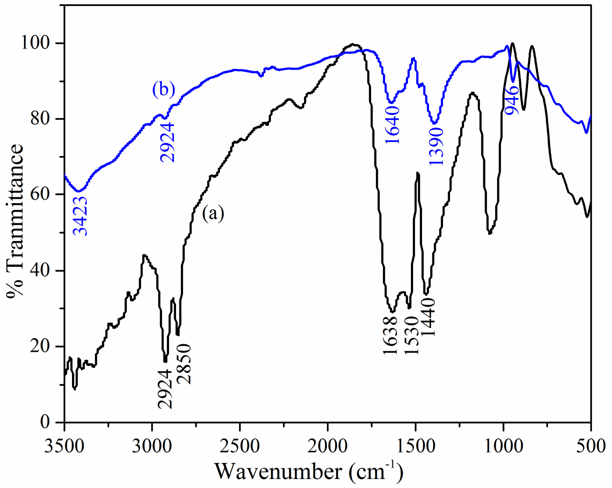

Figure 3.6 Comparative FTIR spectra of (a) hydrophobic and (b) hydrophilic of FePt nanodots

Other peaks in the low-frequency region of the spectra below 1400 cm^{-1} arise from other combinations that are too complex to assign. After phase transfer with TMAOH, the intensity of oleyl group peaks are drastically reduced indicating successful transformation from hydrophobic to the hydrophilic phase of FePt nanodots [32]. An intense and broad band centered at 3423 cm^{-1} region, corresponding to the O-H stretching vibration [26]. The bands around 2924, 1390 cm^{-1} are assigned to the C-H and CH_3 antisymmetric stretching and bending vibrations of TMAOH respectively. Another vibrational feature at 1640 and 946 cm^{-1} is assigned to the C-N stretching vibration and asymmetrical band of TMAOH molecules respectively [27].

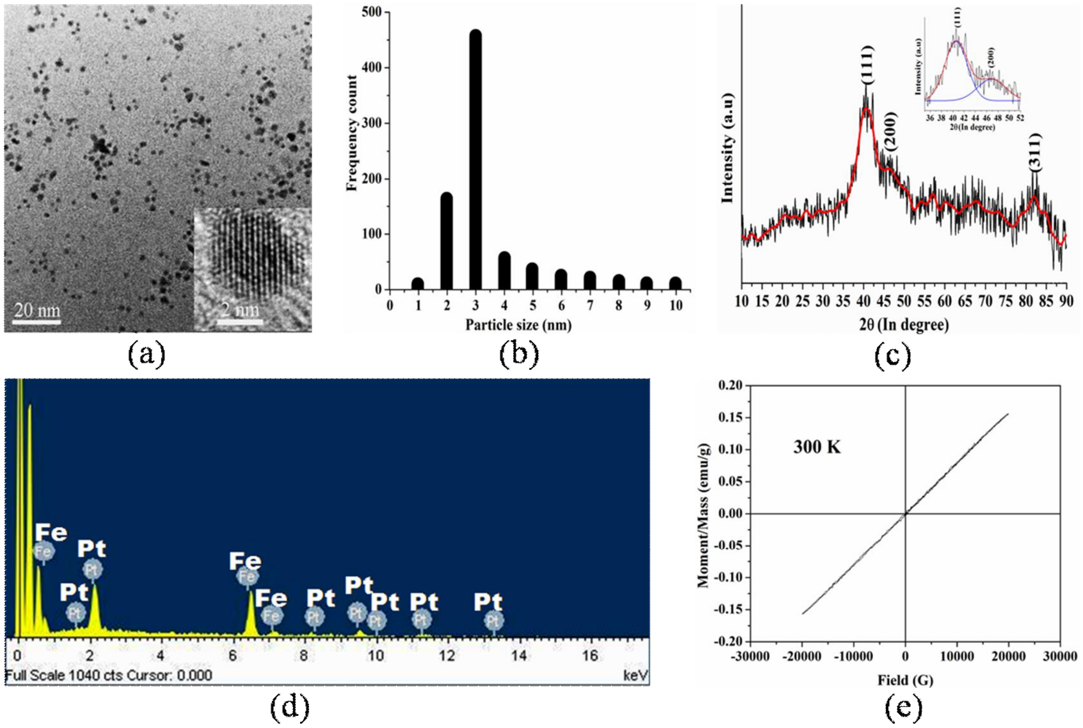

(a) (b) (c)

(d) (e)

Figure 3.7 (a) HR-TEM micrograph (inset showing nanodot), (b) Estimated size distribution, (c) XRD pattern (inset showing deconvolved main peak), (d) EDX pattern and (e) Room temperature hysteresis behavior of hydrophilic FePt nanodots

The HR-TEM micrograph of hydrophilic FePt nanodots has been shown in **figure 3.7 (a)** and the size distribution estimated from the micrograph is shown in **figure 3.7 (b).** The average particle size is ~ 3.5 nm, exhibiting a narrow size distribution. Nanodots, as evident from **figure 3.7 (a**), have nearly spherical shape with uniform dispersion. The narrow size distribution with uniform dispersion could be achieved through the controlled growth of nanodots under reduced synthesis temperature. The addition of $NaBH_4$ facilitates the reduction of the precursors at a lower temperature by lowering the activation energy. This in turn helps to prevent the thermo-aggregation of nanodots to form larger agglomerates, typical to polyol processes, and also facilitates the efficient capping of the nucleating FePt nanodots. The XRD pattern analysis in **figure 3.7 (c)** confirms the phase of face-centered cubic (FCC) FePt nanodots. The pattern shows the presence of peaks at $2\theta \sim 40.5^{\circ}$, 46.4°, and 82.1°corresponding to (111), (200) and (311) orientation of FePt [41]. A pattern decomposition procedure using a pseudo-Voigt profile shape function and subsequent single line analysis, based on equivalent Voigt representation, was used for the determination of crystallite size and lattice strain [42]. Here,

$$D = ә/б^{f}_{c}\mathrm{Cos}ɗ \qquad \text{and} \qquad e = б^{f}_{G}/4\mathrm{tan}ɗ$$

where, D is crystallite size, e is lattice strain, ә is the wavelength of X-ray, $б^{f}_{c}$ and $б^{f}_{G}$ are the integral breadths of Cauchy and Gaussian fit of the structurally broadened profile and ɗ is the Bragg angle. The volume-weighted mean crystallite size of FePt is found to be 2.5 nm and the corresponding lattice strain is 0.0087. This result is in close agreement with the HR-TEM analysis. The EDX of the FePt nanodots as shown in **figure 3.7 (d)** indicates that the energy bands from both Fe (L line, 0.7 keV; $K_{Ǔ}$ line, 6.4 keV; $K_{б}$ line, 7.1 keV) and Pt ($M_{Ǔ\,б}$ line, 2.1 keV; $L_{Ǔ}$ line, 9.4 keV; $L_{б}$ line, 11.1 keV) are present. Compositional analysis was done with five randomly selected FePt nanodots using EDX. We find that the atomic ratio of the nanodots varied around $Fe_{70}Pt_{30}$ (**table-3.1**). **Figure 3.7 (e)** shows the hysteresis behavior of the as-synthesized FePt nanodots at room temperature. The low coercivity and remanence is attributed to the magnetically soft fcc FePt nanodots as well as its superparamagnetic characteristics [43, 44]. This typical superparamagnetic characteristic can be realized by the fact that the thermal energy can overcome the anisotropy energy barrier of the individual particles, and the net magnetization of these nanoparticle assemblies is zero in the absence of an external field. This Fe-rich FePt system should ideally exhibit high biocompatibility and dispersibility thus making it a suitable precursor for the bio-imaging application. In FePt alloy nanosystem, Pt atom is conjugated with Fe atom. Here, these FePt nanoparticles are capped with the biocompatible surfactant. Due to surfactant the toxicity of Pt atom is compromised.

Table 3.1 Compositional analysis of FePt nanodots

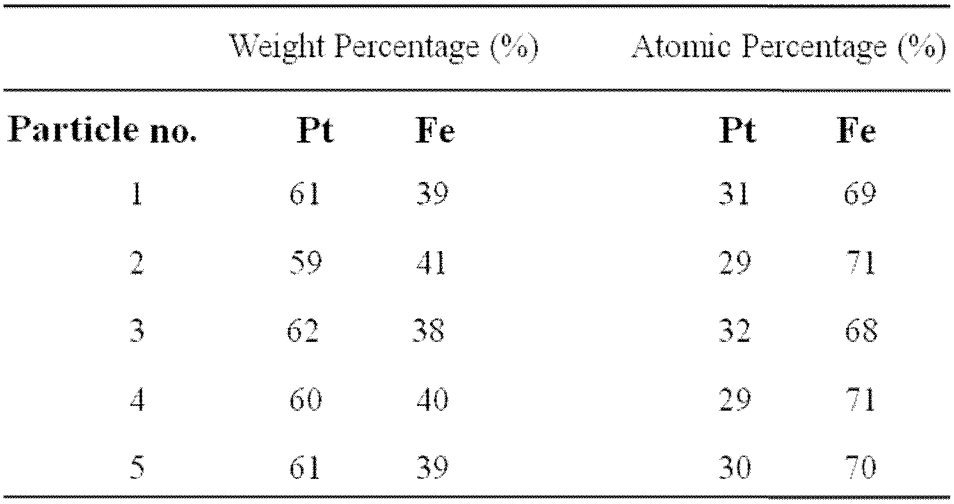

	Weight Percentage (%)		Atomic Percentage (%)	
Particle no.	**Pt**	**Fe**	**Pt**	**Fe**
1	61	39	31	69
2	59	41	29	71
3	62	38	32	68
4	60	40	29	71
5	61	39	30	70

The MRI contrast property of the nanodots was evaluated by monitoring the transverse relaxation time (T_2) of water at 25°C with five different concentrations of the FePt ferrofluid (0.5, 1.0, 2.0, 8.0 and 16.0µg/mL). The spin echo image of the microfuge tube containing water was acquired with different echo time at 14.1 T NMR Micro imager using TR = 6s and TE in the range of 7 ms to 600 ms. As shown in **figure 3.8 (a)** MR image intensity decreases with an increase in echo time. The water signal intensity decreases with increase in echo time and follows an exponential function as evident from **figure 3.8** (b). The MRI signal intensities with different echo time were fitted to a single exponential function $[S_{TE} = S_{TE=0}\ (e^{-TE/T_2})]$ to derive T_2. Transverse relaxation rate ($R_2=1/T_2$) was calculated and plotted against nanodot content in the medium. R_2 increases linearly with an increase in concentration as observed in **figure 3.8 (c).** The transverse relaxivity of the nanodots was found to be 4.42 ml s^{-1} μg^{-1} which makes it a promising T_2 contrast agent for MRI applications.

We have developed a biocompatible ferrofluid for magnetic imaging, comprising of iron-rich FePt nanodots. The native Fe_xPt_{1-x} (x=0.7) nanodots were surface modified to bring about the hydrophobic-hydrophilic phase transformation. Our results provide an alternative approach to synthesize high quality nanoparticles using the polyol process and yet achieve wettable dispersions with high biocompatibility characteristics. Further, the contrast enhancement of the ferrofluid makes it a potential T_2 contrast agent for MRI application.

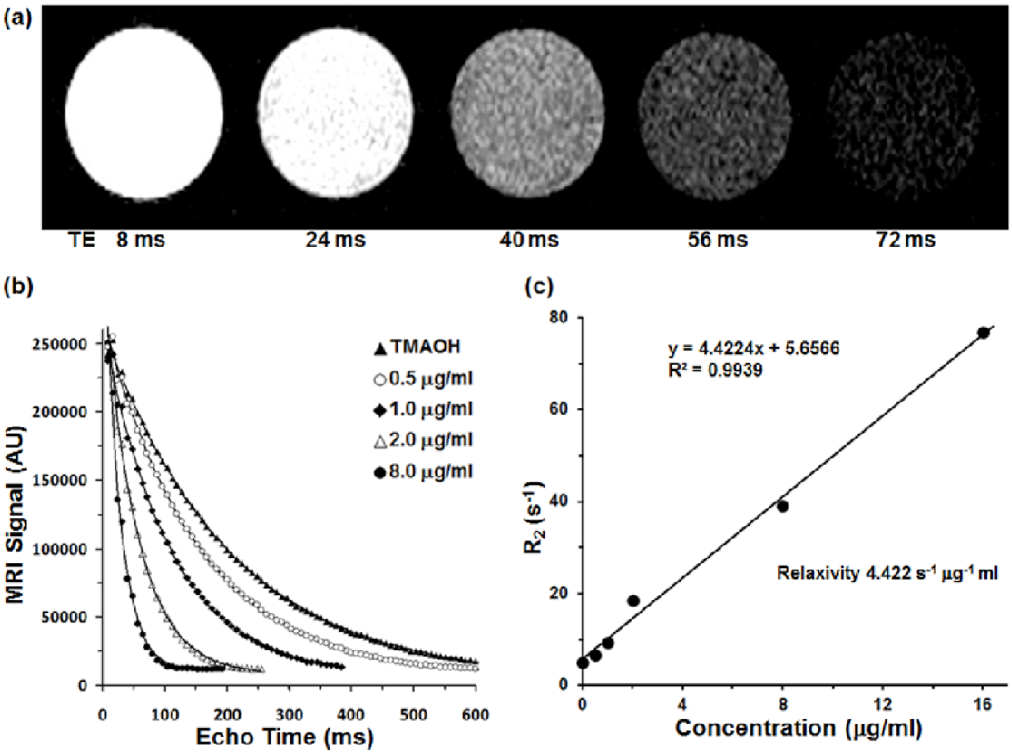

Figure 3.8 Measurement of transverse relaxivity of FePt nanodots. (a) MR image of microfuge tube containing FePt nanodots in water at different echo time (8, 24, 40, 56 and 72 ms), (b) Plot of MR image intensity vs echo time for estimation of transverse relaxation time (T_2) and (c) Variation in transverse relaxation rate w. r. t. nanodot concentrations

In the next section, we will discuss about one pot synthesis of TGA capped hydrophilic FePt magnetic nanoparticles (MNPs). The TGA coated FePt MNPs were used for the development of magneto-fluorescent multimodal hybrid nanosystem.

Section-C

3.7 One pot synthesis of TGA capped hydrophilic FePt nanoparticles:

This experimental series aims to understand the role of a capping agent in the direct synthesis of hydrophilic FePt MNPs. These series of experiments were carried by process-A, B and C. For the direct synthesis of hydrophilic FePt MNPs by facile polyol process-A, initially ethylene glycol (25 ml), 1.0 mmol platinum (II) acetylacetonate, and 4 mmol sodium borohydride were added in a three-necked flask under N_2 atm. at room temperature. After attaining the temperature 100°C, 2 mmol of the iron precursor, iron

(III) acetylacetonate, was added along with surfactant 200 µl (2.75 mmol) of thioglycolic acid (TGA) [31]. TGA prevents the oxidation and agglomeration of as prepared MNPs. The solution was kept under N_2 atm. and heated up to 190 °C at the rate of 1 °C per min. When the reduction of iron salt started, the solution color transformed to black, indicating the complete reduction. Finally, the solution was cooled down to room temperature under inert atmosphere. The FePt precipitate was separated from the reaction mixture by centrifugation and washed several times using acetone, ethyl alcohol and Milli-Q water to remove the residual surfactant. The purified mass obtained through the process-A was named as FePt-A MNPs. In other experiments, named as process-B and process-C, the same synthetic procedure of process-A was followed, except the concentration of TGA. The concentrations were 1.5 and 2 times more in process-B and process-C respectively. The purified product collected from the process-B was named as FePt-B MNPs.

3.8 Characterizations

The synthesized nanosystem was characterized using several characterization methods for understanding the properties of the nanosystems.

3.8.1 Results and discussion

In the synthesis process of A, B, and C, the same molar ratio of Fe: Pt: $NaBH_4$ (2: 1: 4) was taken whereas the molar ratio of TGA was varied. The detailed description of precursors in different synthesis processes has been described in **table-3.2**. The three nanosamples, with the different surfactant to iron ratio (TGA/Fe), were characterized to understand the nucleation and growth of FePt MNPs. **Figure 3.9 (a-c)** reveals XRD pattern of as-synthesized nanoparticles. It is worthwhile to mention that the reducing agent enables faster reduction of metallic precursor and hence faster nucleation of FePt of takes place, resulting in the formation of smaller sized nanoparticles [45, 46]. In these facile polyol processes A-C, $NaBH_4$, ethylene glycol, and TGA combinatorially acted as reducing agents. A careful observation of XRD patterns reveals the formation of fcc-FePt in process-A and process-B samples while there is no signature peak of FePt crystal plane for process-C. The XRD pattern analysis of the sample obtained from process-A exhibits lattice planes (111), (200), (220) and (311) oriented at 2θ values of 40.34°, 46.88°, 68.72° and 82.74° respectively.

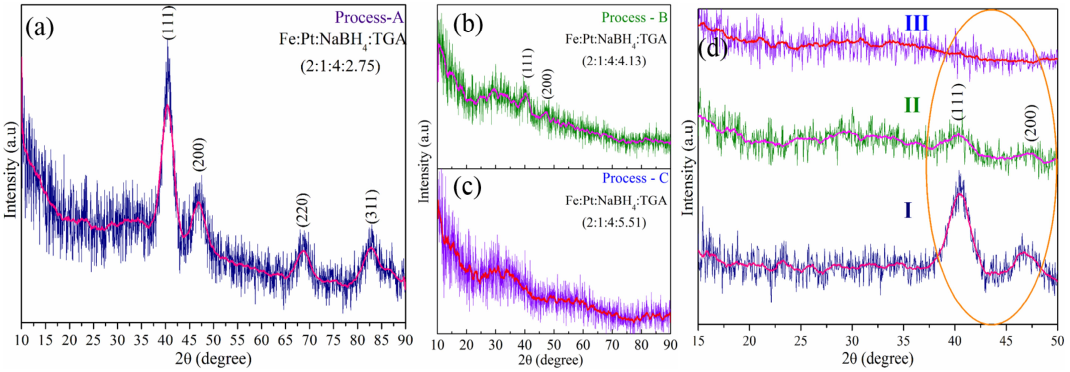

Figure 3.9 XRD patterns of as-prepared samples obtained from (a) process-A (b) process-B (c) process-C. The magnified patterns (2θ = 15 to 50 degree) of the samples, process A (I), B (II), and C (III), are shown in (d)

The sample prepared through process-B exhibits only (111) and (200) lattice planes at 2θ values of 40.05° and 47.08° respectively. **Figure 3.9 (d)** depicts magnified XRD patterns of samples obtained by process-A, B, and C, indicating the absence of signature face centered tetragonal (FCT) lattice planes in FePt MNPs [47]. It also indicates that there is no crystalline peak present in the sample obtained through process-C (III). The crystallinity of sample obtained by process-A (I) is superior to process-B (II) as evident from **figure 3.9 (d).**

Table 3.2 Variation of precursors in synthesis processes A, B, & C

Si. No	Process	Fe Source [Fe(acac)$_3$]	Pt Source [Pt(acac)$_2$]	Reducing Agent [NaBH$_4$]	Capping Agent [TGA]	TGA/Fe [Ratio]	Product
1	Process-A	2 mmol	1 mmol	4 mmol	2.75 mmol	1.37	FePt-A
2	Process-B				4.13 mmol	2.06	FePt-B
3	Process-C				5.51 mmol	2.75	- - - -

The procedures for FePt MNPs synthesis in process-A, B and C were similar except the ratio of surfactant (TGA) to iron metal precursor (Fe(acac)$_3$). This helps to reveal the effect of TGA in FePt MNPs synthesis. When the molar ratio of surfactant to iron metal precursor was 1.37 in the process-A, the highest crystallinity of FePt was obtained. This ratio becomes 2.06 and 2.75 in the process-B and C respectively. When TGA/Fe ratio was increased from process A to B, the number of signature peaks for FePt reduced and a shift in (111) peak is observed. This signifies less diffusion of Fe atoms in the Pt seed, hence reducing the probability of FePt formation [48]. In the process-C, the TGA/Fe ratio becomes double as compared to process-A. The obtained XRD pattern indicates that there is no formation of FePt crystal, which may be either due to the absence of Fe nucleation or steric hindrance posed by Pt seed or both. Here, the capping of TGA may be dominant over Fe nucleation or diffusion of Fe atoms in the Pt seed. As a result, the synthesis of FePt failed. In the present synthesis process, nucleation of Pt occurs initially and then Fe atom nucleates at higher temperature followed by diffusion in Pt seed with subsequent capping by TGA molecules. The sample prepared through the process-A was identified for onward study based on its superior crystallinity and stability. **Figure 3.10** represents a mechanistic model of the synthetic route and the role of surfactant (TGA) in FePt MNPs formation. The merit of usage of TGA in this one step synthesis procedure lies in many fold e.g. TGA providing hydrophilic functionality, superparamagnetic characteristic and provide carboxylate group projected outward to the surface which will help in core/shell or hybrid formation further.

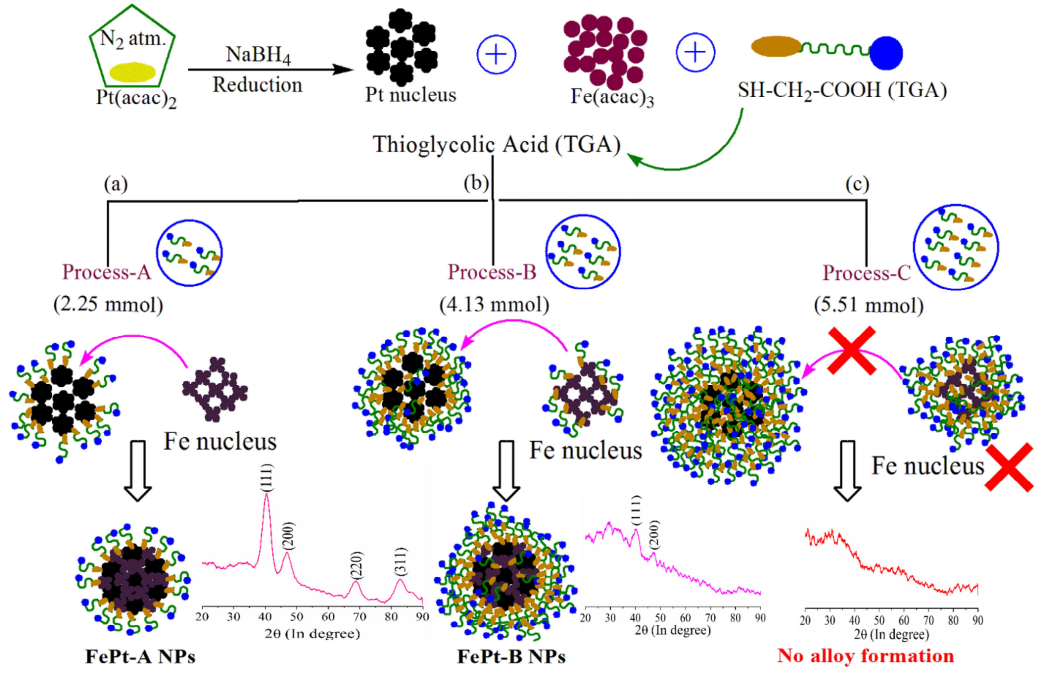

Figure 3.10 schematic mechanistic diagrams representing the effect of capping agent (TGA) on the synthesis of FePt MNPs

The TGA linking on the surface of FePt-A MNPs was investigated by FTIR, zeta-potential and thermogravimetric (TG) analysis. The FTIR spectrum is depicted in **figure 3.11 (a).** It has strong band centered at 3425 cm^{-1} corroborating hydroxyl stretching emerging from TGA and adsorbed water molecules. The peak at 2925 cm^{-1} corresponds to C-H stretching band. The band at 1635 cm^{-1} and 1395 cm^{-1} are due to C=O and C-OH stretching vibration. The band at 1125 and 1035 cm^{-1} can be ascribed as C-O stretching vibration arising from carboxyl ïC(=O)OH group of TGA molecules. The C-S stretching is expressed by the band observed at 603 cm^{-1}[49]. The fundamental S-H and C-S stretching vibrations in the range of 2500-2650 cm^{-1} is not noticed. This suggests that the thiol group of the TGA molecule coordinates with the surface of FePt MNPs and the carboxyl group of TGA molecule renders hydrophilicity to the nanoparticles. **Figure 3.11 (b)** elucidates zeta potential of water dispersible solution within the pH range of 4-12. Higher the absolute value of zeta potential, higher the electrostatic repulsion between MNPs, resulting in the greater degree of dispersion. The figure shows negative potential values over the pH range of 4 to 12. The zeta potential values are -14.1, -27.1, -31.1, -65.3 and -44.3 mV at 4.0, 7.0, 9.0, 10.0, and 12.0 pH respectively. It indicates the long-term stability of sample within the pH range of 9-12.

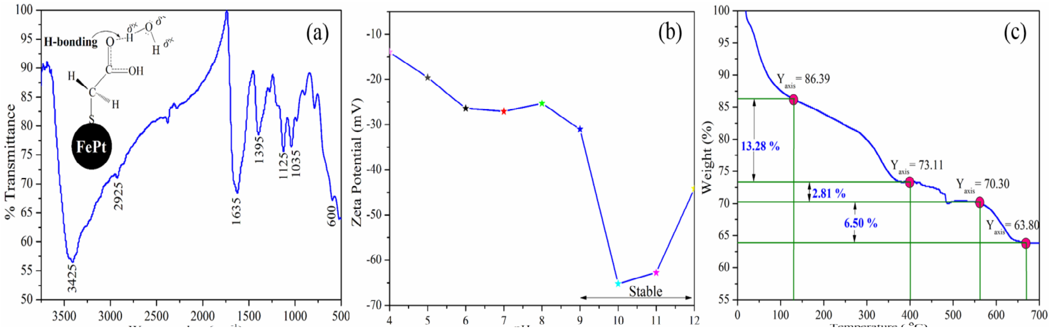

Figure 3.11 (a) FTIR spectrum (Inset model shows the arrangement of TGA molecule on FePt-A MNPs) (b) zeta potential and (c) thermogravimetric (TG) analysis of as prepared FePt-A MNPs

Figure 3.11 (c) indicates the TG analysis of TGA capped FePt MNPs. A weight loss of ~ 14 % is observed up to 130 °C, probably due to evaporation of residual moisture in the sample. The subsequent weight loss of approx. 14 % between 130-400 °C corresponds to desorption of carboxyl group of TGA molecules [50]. A small ~ 3% weight loss within 400-560 °C is probably due to -CH_2 group degradation. The subsequent weight loss of approx. 6.5 % between 560-670 °C is probably due to degradation of Fe-S or Pt-S bond at the interface between FePt and TGA molecules.

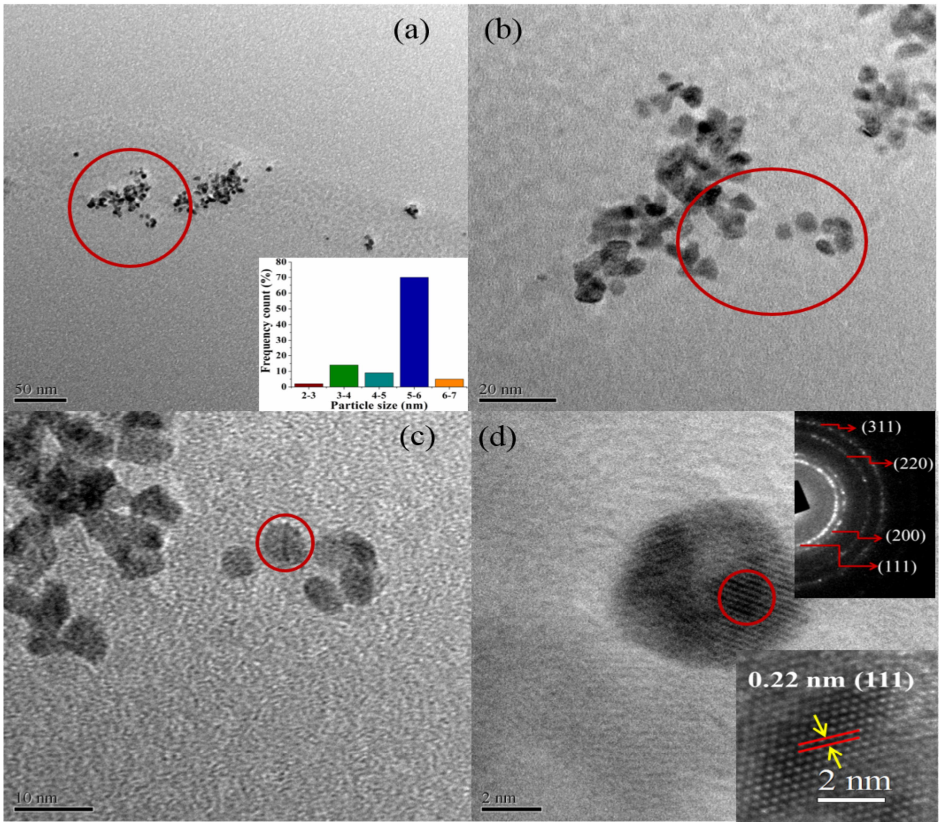

Figure 3.12 TEM image of FePt-A MNPs. The red circle marked image part is magnified in subsequent figures (a) FePt MNPs, inset shows the particle-size distribution histogram, after counting 500 individual particles, (b) and (c) magnified part of previous image (a) and (b) respectively, (d) the single particle. The upper and lower inset of (d) indicate selected area electron diffraction (SAED) pattern and lattice plane of FePt nanocrystals

The primary micrograph and the subsequent magnified micrographs of **figure 3.12 (a-c)**, apparently shows well dispersed spherical particles of FePt-A sample. The average particle size is found to be 2-7 nm with a narrow size distribution 5±1 nm. In the **figure 3.12 (d)**, the SAED pattern reveals the presence of (111), (200), (220) and (311) planes corresponding to FCC phase of FePt NPs. The d value is found to be 0.22 nm from the lattice image and is corroborating to (111) plane of FePt.

The comprehensive composition is expressed in **figure 3.13**. The EDX spectrum of FePt-A MNPs indicates the energy bands from Fe (L line, 0.7 keV; KŬ line, 6.4 keV; Kɓ line, 7.1 keV), Pt (MŬ, ɓ line, 2.1 keV; LŬ line, 9.4 keV; Lɓ line, 11.1 keV), C (KŬ line, 0.2 keV), O (KŬ line, 0.5 keV) and S (KŬ line, 2.3 keV).

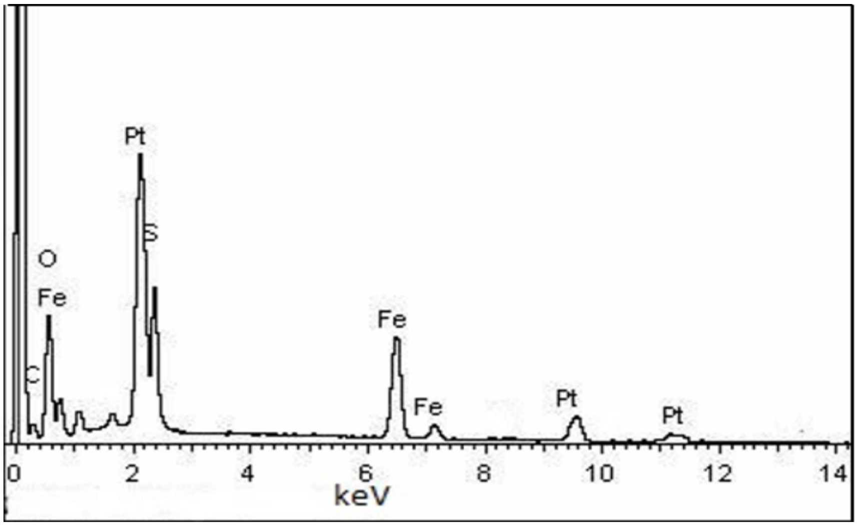

Figure 3.13 EDX spectrum of FePt-A nanoparticles

To ensure uniform composition, the EDX spectrum was recorded from five different locations of the sample and has been shown in the **table-3.3**.

Table 3.3 Compositional analysis of FePt-A MNPs

Scan Area	Weight Percentage (%)		Atomic Percentage (%)	
	Fe	Pt	Fe	Pt
1	22.53	77.47	50.39	49.61
2	22.79	77.21	50.76	49.24
3	22.52	77.48	50.38	49.62
4	22.54	77.46	50.40	49.60
5	22.53	77.47	50.39	49.61

The particles exhibit an almost equiatomic ratio of Fe and Pt. The other elements correspond to the functional group elements of TGA attached to the surface of MNPs.

In the **Figure 3.14 (a)**, the M-H curves of FePt-A MNPs, exhibits saturation magnetization ~7 emu/gm at room temperature, and it increases with decreasing temperature.

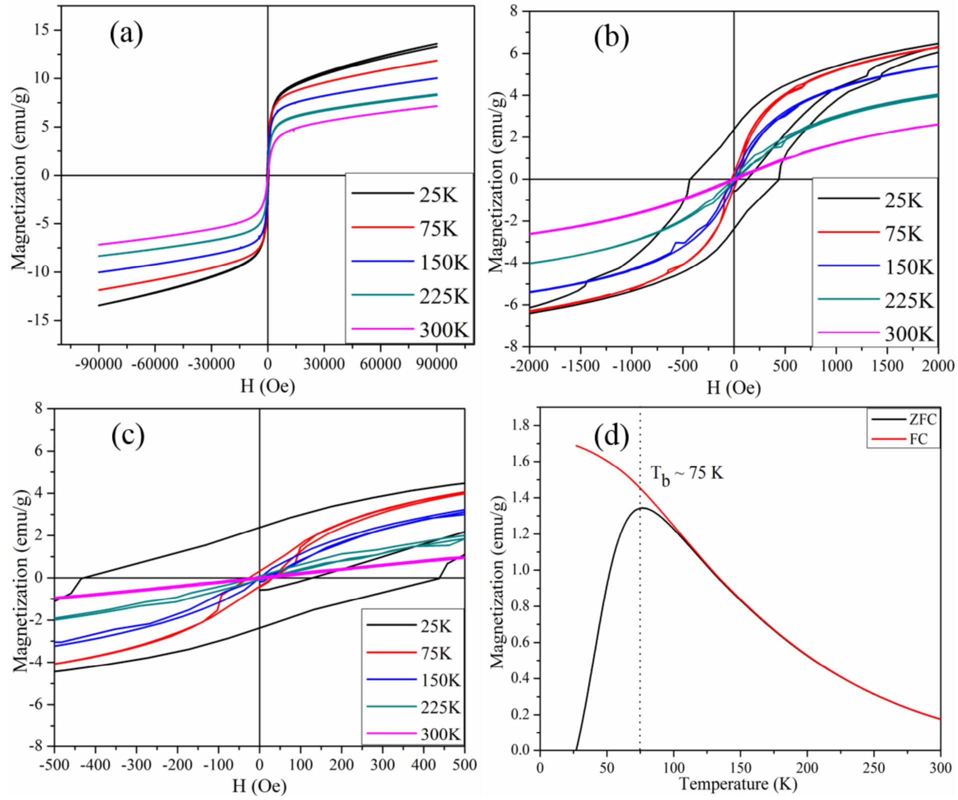

Figure 3.14 Magnetization characterization of FePt-A MNPs (a-c) M-H curves at different temperatures of as prepared FePt-A MNPs. (d) magnetization versus temperature curve measured under ZFC and FC condition

The increased saturation magnetization with decreasing temperature can be corroborated with a decrease in thermal energy. The obtained lower value of saturation magnetization at room temperature as compared to its bulk counterpart could be due to defect induced disordered spin structure. It is also observed that the coercivity increases with decreasing temperature and attains the maximum at 25 K (**figure 3.14 (b-c)).** The observed trend can be explained based on the constrained spin reversal process with lowering of the measurement temperature. **Figure 3.14 (d)** elucidates the M-T measurements (ZFC and FC) of FePt-A nanosystem with probe field at 100 Oe. Observed blocking temperature (75 K) well below the room temperature and increasing trend of FC moment below the blocking temperature correspond to the superparamagnetic character of the FePt-A MNPs. Moreover, the observed Curie behavior of ZFC and FC curves above the blocking temperature implies the negligible interparticle interaction among FePt-A MNPs. The FePt-B MNPs exhibits less saturation magnetization as compared to FePt-A MNPs. The detailed magnetic property of FePt-B is discussed in **3.2A of appendix–A.** The toxicity assay of FePt-A MNPs was examined using toxicity assay by resazurin reduction method. It represents good biocompatibility with RAW macrophage cell line. The result of toxicity assay is explained in **3.3A of appendix–A.**

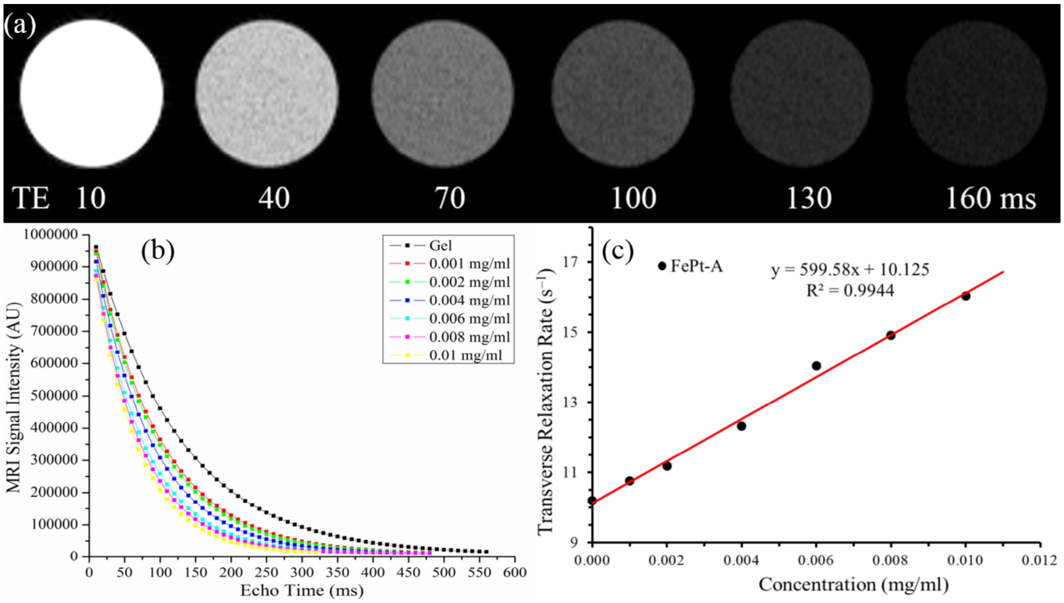

Figure 3.15 Transverse relaxivity characterization (a) typical MR images of microfuge tube containing FePt (0.01 mg/ml in 0.5% agarose gel), (b) estimation of transverse relaxation time (T_2) of water, (c) transverse relaxivity of FePt-A in 0.5% agarose gel

The effect of FePt-A nanoparticles on the spin-spin relaxation times (T_2) of water was studied. The transverse relaxivity measurement was carried out in 0.5% agarose solution. The axial magnetic resonance images (MRI) of microfuse tube containing FePt nanoparticles in Agarose Gel (0.5%) were obtained with varying echo times using multi-slice multi-echo (MSME) protocol (**refer figure 3.15 (a)**). The MRI signal intensity with echo time was analyzed for a mono-exponential function ($[S_{TE}=S_{TE=0}\ (e^{-TE/T_2})]]$) to derive T_2. The measurements of water T_2 was carried out with varying concentration of FePt nanoparticles (**refer figure 3.15 (b)**). The transverse relaxivity (R_2) of FePt nanoparticles was estimated from the plot of relaxation rate (reciprocal of

T_2) of the water against the iron content in the nanoparticles. The relaxivity (r_2), measures of the change in the spinï spin relaxation rate per unit concentration, is found to be 599.6 s^{-1} mg^{-1} ml for the FePt nanoparticles (R^2 =0.994) (**refer figure 3.15** (**c**)). The transverse relaxivity of FePt nanoparticles is extraordinary to that of protein-polymer functionalized iron oxide nanoparticles [51]. This simple approach could be used to improve, relaxation properties of contrast materials for biomedical applications.

3.9 Conclusion

The magnetic nanosystems, magnetite (Fe_3O_4) and iron-platinum (FePt) have been developed through facile routes and subsequently characterized. A facile, one-pot and open environment non-aqueous thermal decomposition method has been developed to synthesize monodisperse superparamagnetic Fe_3O_4 NPs. Surface modification by TMAOH treatment yields water dispersible superparamagnetic magnetite NPs. This monophasic replacement of fatty acid by TMAOH on the surface of NPs does not lead to any notable change in the microstructure and phase. A high transverse relaxivity of obtained magnetite NPs has been observed for MRI contrast application. We have also developed a biocompatible ferrofluid for magnetic imaging, comprising of iron-rich FePt nanodots. The native Fe_xPt_{1-x} (x=0.7) nanodots were surface modified to bring about the hydrophobic-hydrophilic phase transformation. Our results provide an alternative approach to synthesize high-quality nanoparticles using the polyol process and yet achieve wettable dispersions with high biocompatibility characteristics. Further, the contrast enhancement of the ferrofluid makes it a potential T_2 contrast agent for MRI application. In another attempt, superparamagnetic hydrophilic FePt MNPs with controlled microstructure were successfully prepared via a facile one-pot method, in which TGA was used as reducing agent, capping agent and stabilizer simultaneously. This direct synthesis procedure offers a several advantageous feature like cost-effectivity due to reduced number of steps, better aqueous dispersion with high stability and scope for large-scale synthesis in a single step. The so-prepared FePt MNPs system was characterized to evaluate microstructure, functionality, and magnetic properties. Moreover, FePt-A MNPs system exhibited notable MRI transverse relaxivity. It is realized that TGA capped FePt nanoparticles provide projected carboxylate groups which act as binding sites for Cd^{2+} and promote the CdX shell growth while capping with TMAOH is not suitable for such shell growth possibility. Therefore, the MNP systems stabilized with TMAOH have been not used further for the hybrid formation. The TGA capped FePt MNPs were used as a core for the multimodal core-shell hybrid nanosystems like FePt@X (X= CdTe, CdSe, CdS).

References:

[1] Sun, C. *et al.* Magnetic nanoparticles in MR imaging and drug delivery. *Advanced Drug Delivery Reviews* **60** (11), 1252--1265, 2008.

[2] Jha, D. K. *et al.* Simple synthesis of superparamagnetic magnetite nanoparticles as highly efficient contrast agent. *Mater. Lett.* **95,** 186--189, 2013.

[3] Murphy, C. J. *et al.* Gold nanoparticles in biology: Beyond toxicity to cellular imaging. *Acc. Chem. Res.* **41** (12), 1721--1730, 2008.

[4] Weissleder, R. *et al*. Imaging macrophages with nanoparticles. *Nat. Mater.* **13** (2), 125--38, 2014.

[5] Lee, DE. *et al.* Multifunctional nanoparticles for multimodal imaging and theragnosis. *Chemical Society Reviews* **41** (7), 2656, 2012.

[6] Nune, S. K. *et al.* Nanoparticles for biomedical imaging. *Expert Opin. Drug Deliv.* **6** (11), 1175--1194, 2009.

[7] McCarthy, J. R. & Weissleder, R. Multifunctional magnetic nanoparticles for targeted imaging and therapy. *Advanced Drug Delivery Reviews* **60** (11), 1241--1251, 2008.

[8] Hammel, P. C. Imaging: nanoscale MRI. *Nature* **458** (7240), 844--845, 2009.

[9] Portalez, D. *et al.* Prospective comparison of T2w-MRI and dynamic-contrast-enhanced MRI, 3D-MR spectroscopic imaging or diffusion-weighted MRI in repeat TRUS-guided biopsies. *Eur. Radiol.* **20** (12), 2781--2790, 2010.

[10] Glover, P. & Bowtell, R. Medical imaging: MRI rides the wave. *Nature* **457** (7232), 971--972, 2009.

[11] Jasanoff, A. Functional MRI using molecular imaging agents. *Trends in Neurosciences* **28** (3), 120--126, 2005.

[12] Na, H. Bin, *et al.* Inorganic nanoparticles for MRI contrast agents. *Adv. Mater.* **21** (21), 2133--2148, 2009.

[13] Tromsdorf, U. I., *et al.* A highly effective, nontoxic T1 MR contrast agent based on ultrasmall PEGylated iron oxide nanoparticles. *Nano Lett.* **9** (12), 4434--4440, 2009.

[14] Horak, D. *et al.* D-mannose-modified iron oxide nanoparticles for stem cell labeling. *Bioconjug. Chem.* **18** (3), 635--44, 2007.

[15] Ling, D. & Hyeon, T. Chemical design of biocompatible iron oxide nanoparticles for medical applications. *Small* **9** (9), 1450--1466, 2013.

[16] Lee, N. & Hyeon, T. Designed synthesis of uniformly sized iron oxide nanoparticles for efficient magnetic resonance imaging contrast agents. *Chemical Society Reviews* **41** (7), 2575, 2012.

[17] Chaianansutcharit, S. *et al.* Effect of Organic Solvents on Iron Oxide Nanoparticles by the Solvothermal Method. *Cryst. Growth Des.* **6** (1) , 40--45, 2006.

[18] Liang, MT. *et al.* Iron oxide synthesis using a continuous hydrothermal and solvothermal system. *Ceramics International* **36** (3), 1131--1135, 2010.

[19] Gnanam, S. & Rajendran, V. Synthesis of tin oxide nanoparticles by solï gel process: effect of solvents on the optical properties. *J. Sol-Gel Sci. Technol.* **53** (3), 555--559, 2009.

[20] Cividanes, L. S. *et al*. Review of mullite synthesis routes by sol-gel method. *J. Sol-Gel Sci. Technol.* **55** (1), 111--125, 2010.

[21] Sun, S. Monodisperse FePt Nanoparticles and Ferromagnetic FePt Nanocrystal Superlattices. *Science* **287** (5460), 1989--1992, 2000.

[22] Chen, M. *et al.* One-step synthesis of FePt nanoparticles with tunable size. *J. Am. Chem. Soc.* **126** (27), 8394--8395, 2004.

[23] Chen, S. & Andre, P. Colloidal syntheses of FePt nanoparticles. *International Journal of Nanotechnology* **9** (1), 39--68, 2012.

[24] De Palma, R. *et al.* Silane ligand exchange to make hydrophobic superparamagnetic nanoparticles water-dispersible. *Chem. Mater.* **19,** (7), 1821--1831, 2007.

[25] Zhang, T. *et al.* A general approach for transferring hydrophobic nanocrystals into water. *Nano Lett.* **7,** (10), 3203--3207, 2007.

[26] Saha, A. *et al.* Ligand exchange approach in deriving magnetic-fluorescent and magnetic-plasmonic hybrid nanoparticle. *Langmuir* **26,** (6), 4351--4356, 2010.

[27] Ko, Y. *et al.* Hydrophobic nanoparticle-based nanocomposite films using in situ ligand exchange layer-by-layer assembly and their nonvolatile memory applications. *ACS Nano* **7,** (1), 143--153, 2013.

[28] Dong, A. *et al.* A generalized ligand-exchange strategy enabling sequential surface functionalization of colloidal nanocrystals. *J. Am. Chem. Soc.* **133,** (4), 998--1006, 2011.

[29] Caragheorgheopol, A. & Chechik, V. Mechanistic aspects of ligand exchange in Au nanoparticles. *Phys. Chem. Chem. Phys.* **10,** (33), 5029--5041, 2008.

[30] Yang, H. *et al.* One-pot synthesis of amphiphilic superparamagnetic FePt nanoparticles and magnetic resonance imaging in vitro. *Journal of Magnetism and Magnetic Materials,* **322,** (8), 973--977, 2010.

[31] Jha, D. K. *et al.* Direct synthesis of water dispersible superparamagnetic TGA capped FePt nanoparticles: One pot, one shot. *Mater. Chem. Phys.,* **156,** 247--253, 2015.

[32] Wen, X. *et al.* Preparation of monodisperse magnetite nanoparticles under mild conditions. *Curr. Appl. Phys.* **8** (5), 535--541, 2008.

[33] Qu, Q. *et al.* Chemically binding carboxylic acids onto TiO 2 nanoparticles with adjustable coverage by solvothermal strategy. *Langmuir* **26** (12), 9539--9546, 2010.

[34] Cheng, F. Y. *et al.* Characterization of aqueous dispersions of Fe3O4 nanoparticles and their biomedical applications. *Biomaterials* **26** (7), 729--738, 2005.

[35] Ouasri, A. *et al.* Structure and vibrational study of the trimethylammonium hexafluorosilicate $[(CH_3)_3NH]_2SiF_6$ compound. *Spectrochim. Acta - Part A Mol. Biomol. Spectrosc.* **59** (4), 851--857, 2003.

[36] Mahmoudi, M. *et al.* Optimal design and characterization of superparamagnetic iron oxide nanoparticles coated with polyvinyl alcohol for targeted delivery and imaging. *J Phys Chem B* **112** (46), 14470--14481, 2008.

[37] Oude Engberink, R. D. *et al.* Comparison of SPIO and USPIO for *in vitro* labeling of human monocytes: MR detection and cell function. *Radiology* **243** (2), 467--474, 2007.

[38] Jha, D. K. *et al.* Synthesis and characterization of iron-rich Fe_xPt_{1-x} ferrofluid for magnetic resonance imaging. *Phys. Scr.* **85** (3), 035802, 2012.

[39] Maenosono, S. *et al.* Mutagenicity of water-soluble FePt nanoparticles in Ames test. *The Journal of toxicological sciences* **32** (5), 575--579 2007.

[40] Salgueiriño-Maceira, V. *et al.* Water-based ferrofluids from FexPt1-x nanoparticles synthesized in organic media. *Langmuir* **20** (16), 6946--6950, 2004.

[41] Gupta, G. *et al.* Stable ordered FePt mesoporous silica catalysts with high loadings. *Chem. Mater.* **20** (15), 5005--5015, 2008.

[42] Deb, P. *et al.* Anomalous agglomeration characteristics observed in iron oxide nanoclusters. *Philos. Mag. Lett.* **86** (8), 491--499, 2006.

[43] Seehra, M. S. *et al.* Size-dependent magnetic parameters of fcc FePt nanoparticles: applications to magnetic hyperthermia. *J. Phys. D. Appl. Phys.* **43** (14), 145002, 2010.

[44] Nandwana, V. *et al.* Size and shape control of monodisperse FePt nanoparticles. *J. Phys. Chem. C* **111** (11), 4185--4189, 2007.

[45] Chen, M. *et al*. One-step synthesis of FePt nanoparticles with tunable size. *J. Am. Chem. Soc.* **126** (27), 8394--8395, 2004.

[46] Liu, C. *et al.* Polyol Process Synthesis of Monodispersed FePt Nanoparticles. *J. Phys. Chem. B* **108** (20), 6121--6123, 2004.

[47] Sahu, N. K. *et al.* Role of different platinum precursors on the formation and reaction mechanism of FePt nanoparticles and their electrocatalytic performance towards methanol oxidation. *Dalton Trans.* **43** (12), 4892--900, 2014.

[48] Srivastava, C. *et al.* Formation mechanism and composition distribution of FePt nanoparticles. *J. Appl. Phys.* **102** (10), 104310--104318, 2007.

[49] Xie, R. *et al.* Fe:ZnSe semiconductor nanocrystals: Synthesis, surface capping, and optical properties. *J. Alloys Compd.* **509** (7), 3314--3318, 2011.

[50] Purkayastha, A. *et al.* Molecularly protected bismuth telluride nanoparticles: Microemulsion synthesis and thermoelectric transport properties. *Adv. Mater.* **18** (4), 2958--2963, 2006.

[51] Bhattacharya, S. *et al.* Protein-polymer functionalized aqueous ferrofluids showing high T2 relaxivity. *J. Biomed. Nanotechnol.* **10** (5), 811--819, 2014.